On the Impact of the Acoustic Wave Direction on the In-Orifice Flow Dynamics of an Acoustic Liner Grazed by a Turbulent Flow

On the impact of the acoustic wave direction on the in-orifice flow dynamics of an acoustic liner grazed by a turbulent flow

Angelo Paduano*
Politecnico di Torino, Corso Duca degli Abruzzi 24, 10122, Torino, Italy

Lucas M. Pereira †, Lucas A. Bonomo ‡ and Julio A. Cordioli§
Federal University of Santa Catarina, Florianópolis - SC, 88040-900, Brazil

Damiano Casalino¶
Delft University of Technology, Kluyverweg 1, 2629HS, Delft

Francesco Avallone‖
Politecnico di Torino, Corso Duca degli Abruzzi 24, 10122, Torino, Italy

This study investigates the aerodynamic and acoustic response of a multi-orifice acoustic liner grazed by a planar acoustic wave and turbulent flow, at centerline Mach number equal to 0.32. High-fidelity flow simulations are carried out using a Lattice-Boltzmann Very-Large-Eddy-Simulation solver and the in-situ technique is used to calculate impedance. The triple decomposition technique is adopted to separate the mean-flow effects from those due to grazing tonal acoustic waves with different frequencies and amplitudes. This study highlights the sensitivity of in-situ measurements on the position of the face-sheet probe used to sample the unsteady pressure fluctuations. It is found that the resistance changes up to a factor of three along each cavity. The acoustic-induced velocity field reveals the intricate interaction between the acoustic waves and the turbulent flow. It is shown that the wake shed by the upstream cavity impacts the downstream one, affecting the spatial distribution and the amplitude of the acoustic-induced velocity within the orifice. Furthermore, a vortex within the hole is observed; it is found that its impact on resistance depends on the acoustic wave propagation with respect to the mean flow.

Symbols and Acronyms

Z	=	Impedance
θ	=	Resistance
χ	=	Reactance
L	=	Length of the liner
l	=	Width of each square cavity
τ	=	Face-sheet thickness
ω_p	=	Partition wall thickness
d	=	Orifice diameter
λ	=	Cavity depth
f	=	Frequency
SPL	=	Sound Pressure Level

*PhD student, Department of Mechanical and Aerospace Engineering, angelo.paduano@polito.it.
†PhD student, Department of Mechanical Engineering, lucas.meirelles@lva.ufsc.br, AIAA member.
‡PhD student, Department of Mechanical Engineering, lucas.bonomo@lva.ufsc.br, AIAA member.
§Associate Professor, Department of Mechanical Engineering, julio.cordioli@ufsc.br, AIAA member.
¶Full Professor, Department of Flow Physics and Technology, d.casalino@tudelft.nl, AIAA member.
‖Full Professor, Department of Mechanical and Aerospace Engineering, francesco.avallone@polito.it, AIAA member.

M = Mach number

I. Introduction

Aircraft noise is a significant concern because it impacts the well-being of individuals near airports. Engines are among the most relevant noise sources, especially in take-off conditions. Upcoming Ultra High Bypass Ratio (UHBR) turbo-fan engines are characterized by larger fan diameter, shorter nacelle, lower fan rotational speed, and lower jet core velocity with respect to typical High Bypass Ratio engines. Therefore, fan noise becomes more relevant than jet noise in this scenario. Fan noise is characterized by tones at harmonics of the Blade-Passage Frequency (BPF) and broadband components mostly caused by the interaction between the turbulent wake from the rotor and the stator [1–3].

Conventional acoustic liners are usually employed to mitigate the tonal component. These passive devices often comprise a sandwich structure with a honeycomb core, a perforated face-sheet, and a solid backplate. This design in commonly referred to as a Single Degree Of Freedom (SDOF) liners [4]. Liners are characterized by their acoustic impedance, defined in the frequency domain as the ratio of the acoustic pressure and the acoustic particle velocity normal to the surface [5]. Impedance is therefore a complex number, whose real part is the resistance θ, while the imaginary is the reactance χ. Conventionally, acoustic impedance is normalized with respect to the characteristic impedance of air $Z_0 = \rho_0 c_0$.

In the realm of classical acoustics, liners are commonly regarded as locally reacting, meaning their response hinges solely on the local sound pressure level and particle velocity rather than the angle of incidence of the acoustic wave [4, 6]. Thus, the response of liners depends on various parameters, including geometric features, frequency and amplitude of the acoustic field (the latter expressed in terms of Sound Pressure Level, SPL), and flow conditions. Considerable knowledge exists regarding the impact of geometric factors on the acoustic damping properties of liners [7–9]. Nevertheless, even though the physics of acoustic liners is well-established when they are exposed solely to an acoustic wave [10, 11], a gap persists in understanding and modelling liners subjected to realistic conditions, i.e., in presence of both acoustic wave and grazing turbulent flow at high Mach numbers and high SPL [12–15]. For these cases, a deeper understanding of how the flow interacts with the acoustic wave within the orifices of the face-sheet is still needed [13]. The fact that, in the presence of grazing flow, the physical mechanisms are still rather unclear is further supported by the fact that, for a locally reactive SDOF liner, impedance shall be independent of the direction of propagation of the acoustic wave with respect to the direction of advection of the flow [16, 17]. However, discrepancies have been found experimentally and were attributed to a failure of the boundary conditions adopted to model the liner for impedance eduction. Even if extensive investigations have been conducted to comprehensively incorporate all pertinent physical mechanisms into the boundary conditions [18], some experimental inconsistencies are still found [19].

The interaction between the acoustic-induced flow field and the grazing flow was first visualized by Baumeister and Rice [20]. They demonstrated the presence of flow recirculation near the upstream side of the neck, which resulted in a reduction of space available for flow passage. Later, Hersh and Walker [21] studied experimentally multiple orifices under the influence of grazing flow. They identified the discharge coefficient as a relevant parameter to characterize the response of the liner. The discharge coefficient is defined as the ratio of the area available for flow passage (S_{vc}), which is affected by the flow recirculation within the orifice, to the orifice area ($\pi d^2/4$), thus $C_D = S_{vc}/(\pi d^2/4)$. Similar findings were reported by Zhang and Bodony [13, 22], who studied through Direct Numerical Simulations (DNS) the behaviour of an acoustic liner grazed by turbulent and laminar boundary layers. Their work has unveiled an intricate interaction between the acoustic field and the flow at the interface, corroborating what was previously stated. It is worth noting that the methodology employed did not yield results consistent with the reference experiments [23].

Several semi-empirical models have been developed to predict impedance. Howe [24] developed an expression for the Rayleigh conductivity of an aperture through which a high Reynolds number flow passed through, whereas Cummings [25] established a relation between the acoustic resistance and the discharge coefficient via a quasi-steady model. A semi-empirical model that accounts for linear and non-linear effects was developed by Yu et al. [26]. However, although these methods could predict the trend of reactance and resistance well, they could not closely match experimental results.

This work expands upon earlier numerical investigation carried out by Schroeder et al. [27], Pereira et al. [19] and Pereira [28]. The former examined the response of an acoustic liner grazed by a planar acoustic wave, while the latter investigated a liner grazed by a planar acoustic wave and a turbulent flow. In this paper, we will present high-fidelity numerical simulations carried out with the Lattice-Boltzmann Very-Large-Eddy-Simulation (LB/VLES) solver SIMULIA PowerFLOW®. This solver has been extensively validated and used for aeroacoustic applications, including acoustic liners [3, 29–32]. For the same simulated acoustic liner, physical tests have been carried out, and

measurements are available [33]. Using numerical and experimental results will shed more light on the flow behaviour within the cavity and how it affects impedance.

The rest of the paper is structured as follows: the computational method is summarized in Section II. The computational setup is described in Section III. Section IV reports an overview of the technique used to measure impedance and the adopted post-processing methods. Section Voffers a preliminary validation of the numerical setup. Numerical results compared with experimental data are presented in Section VI. Conclusions are summarized in the last section.

II. Computational method

A. Flow solver

The commercial software 3DS Simulia PowerFLOW version 6 has been used. It is based on the Lattice Boltzmann Method (LBM). The discretized version of the continuous Boltzmann equation, both in space and time, is solved [34]:

$$\frac{\delta g}{\delta t} + \vec{\xi}\frac{\delta g}{\delta x} + F\frac{\delta g}{\delta \vec{\xi}} = \Omega. \tag{1}$$

The distribution function $g(\vec{\xi},\vec{x},t)$ defines the probability for an existing particle at point $[\vec{x}, \vec{x} + \Delta\vec{x}]$ within the time step $[t, t + \Delta t]$ with velocity $[\vec{\xi}, \vec{\xi} + \Delta\vec{\xi}]$. The left side of the equation represents the particles' transport and the influence of external forces, such as gravity, on their behaviour. On the right-hand side the BGK-Collision-Operator [35] describes the interaction between particles:

$$\Omega = -\frac{1}{\tau}(g - g^{eq}); \tag{2}$$

where τ is the relaxation time and g^{eq} is the equilibrium distribution function derived from the Maxwellian-Boltzmann equilibrium distribution.

The distribution of particles is solved by means of the LB equation on a Cartesian mesh, named the lattice; the discrete volume elements are called voxels (vx). Particles can move along discrete directions with discrete velocities at discrete time intervals. Following the standard DkQb model notation [36], where k stands for the dimension of space and b represents the number of discrete velocity directions, a D3Q19 lattice scheme has been employed.

A Very Large Eddy Simulation (VLES) approach has been employed to resolve only the larger turbulence scales. The sub-grid scales are accounted for by adding a turbulent relaxation time to the viscous relaxation time using a turbulence model, based on the two equation Renormalization Group Theory (RNG) $k - \epsilon$ [37] given by

$$\tau_{\text{eff}} = \tau + C_\mu \frac{k^2/\epsilon}{(1+\eta^2)^{1/2}}, \tag{3}$$

where $C_\mu = 0.09$ and η are a combination of the local strain, local vorticity, and local helicity parameters. The term η allows for mitigation of the sub-grid scale viscosity, in the presence of large resolved vortical structures.

The solver uses an extended turbulent wall model that dynamically incorporates the presence of a pressure gradient (PGE-WM) [38]. This model takes into account the effect of the pressure gradient by rescaling the length-scale y^+, in the generalized law-of-the-wall [39], by a scaling parameter A:

$$u^+ = \frac{1}{k} ln\left(\frac{y^+}{A}\right) + B; \tag{4}$$

where $B = 5.0$, $k = 0.41$, $y^+ = (u_\tau y)/\nu$ and A is a function of the pressure gradient. Parameter A captures the physical consequence of the velocity profile slowing down and expanding due to the pressure gradient. The parameter A is defined as proposed by Texeira et al. [38]:

$$A = 1 + \frac{\beta|\frac{dp}{ds}|}{\tau_w}, \quad \boldsymbol{u_s} \cdot \frac{dp}{ds} > 0; \tag{5}$$

$$A = 1, \quad \text{otherwise}; \tag{6}$$

where τ_w is the wall shear stress, dp/ds is the streamwise pressure gradient, and β is a length of the same order of the unresolved near-wall region.

B. Triple Value Decomposition

To gain a comprehensive understanding of how acoustic-flow interaction occurs, it is essential to separate the hydrodynamic effect from acoustic-induced velocity, i.e., to isolate the acoustic-induced component from the turbulent flow fluctuations with the same frequency of the acoustic excitation. To accomplish this, the triple decomposition method has been employed in this study, as detailed by Avallone and Casalino [15].

The method consists of the following steps: the time series extracted from the LB/VLES simulations are initially phase-locked with the incoming acoustic wave; the resultant phase-locked velocity components are denoted as $\tilde{u}$, $\tilde{v}$, $\tilde{w}$. These phase-locked fields are averaged, yielding the corresponding velocity components indicated as $\bar{u}, \bar{v}, \bar{w}$. Subsequently, the acoustic-induced velocity is determined by subtracting the phase-averaged field from the phase-locked fields, denoted as $\bar{\tilde{u}}, \bar{\tilde{v}}, \bar{\tilde{w}}$.

III. Computational Setup

The computational domain, shown in Figure 3 was built to replicate the sample tested at the UFSC Liner Test Rig [33]. The liner is placed in the middle of the channel at the top wall of a duct with a rectangular cross-section. Each cavity has a square cross-section $l = 8.46d$ wide and a depth of $\lambda = 34.18d$, where $d = 1.17$ mm corresponds to orifice diameter. Each cavity has eight orifices, partition walls have a thickness of $w_p = 2.17d$, and the face sheet of the sample is $\tau = 0.46d$. This translates into a cavity Percentage of Open Area (POA) equal to 8.75%. The design of the present sample, though resembling previous studies [19, 28], exhibits variations in terms of the face-sheet thickness, hole diameter and shape of the orifices edges, which were slightly rounded as discerned from a 3D scanning of the real liner sample. The scan also revealed that these parameters were not constant along the sample, due to manufacturing limitations. Therefore, averaged values were considered to build the liner for the numerical simulations.

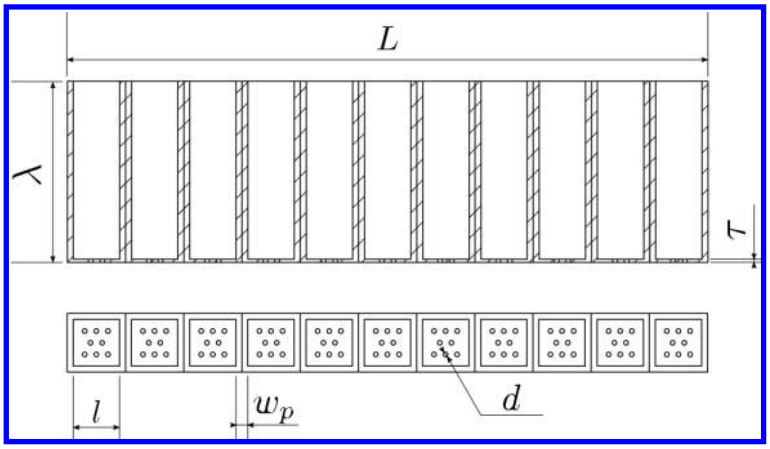

Fig. 1 Schematic representation of the sample.

Only a row of eleven cavities was considered for the simulations, resulting in a stream-wise length of $L = 116.23d$. Periodic boundary conditions were applied on both sides as depicted in Figure 2.

In Figure 3, the entire computational domain employed in the simulations is presented. For the discretization of the domain, a Variable Resolution (VR) scheme has been applied to the lattice grid, providing enhanced refinement in specific regions of the computational domain. Each increase in grid refinement is defined by dividing the size of adjacent cells by a factor of 2.

As shown in the detail in Figure 3, the finest resolution for the mesh was set in the near-wall regions to ensure an accurate solution of the Turbulent Boundary Layer (TBL). Various mesh refinements were simulated to evaluate the convergence: 20, 40, and 80 voxels/d, named Medium, Fine, and Very Fine resolutions, respectively.

In the upstream region, a zig-zag trip has been included on the wall. Its size and position were manually adjusted to achieve a proper match between the experimental velocity profile of the UFSC test rig and the one obtained from the simulation [15]. The zig-zag trip was positioned at $x = -1367d$. The tripping device is $0.21d$ high and $1.71d$ long.

Furthermore, to achieve a quasi-anechoic condition and prevent acoustic perturbation from being reflected at the channel's termination, the fluid's viscosity was significantly increased in the purple regions of Figure 3. Here, the viscosity was increased by a factor of one hundred following an exponential law.

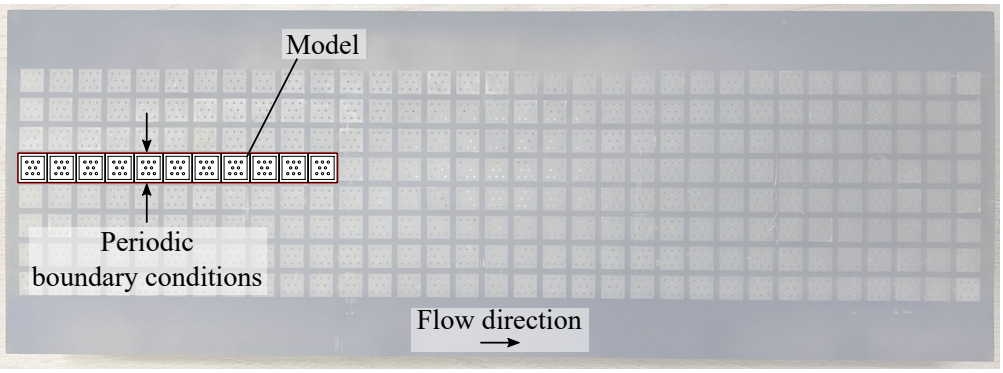

Fig. 2 Comparison between the real UFSC sample and the modelled geometry for the simulations.

All walls in the computational domain were set as adiabatic. The grey and blue colored walls depicted were designed as slip and no-slip boundary conditions, respectively. At the inlet, free-stream velocity corresponding to the free-stream Mach number was assigned, while a pressure boundary condition was set at the outlet.

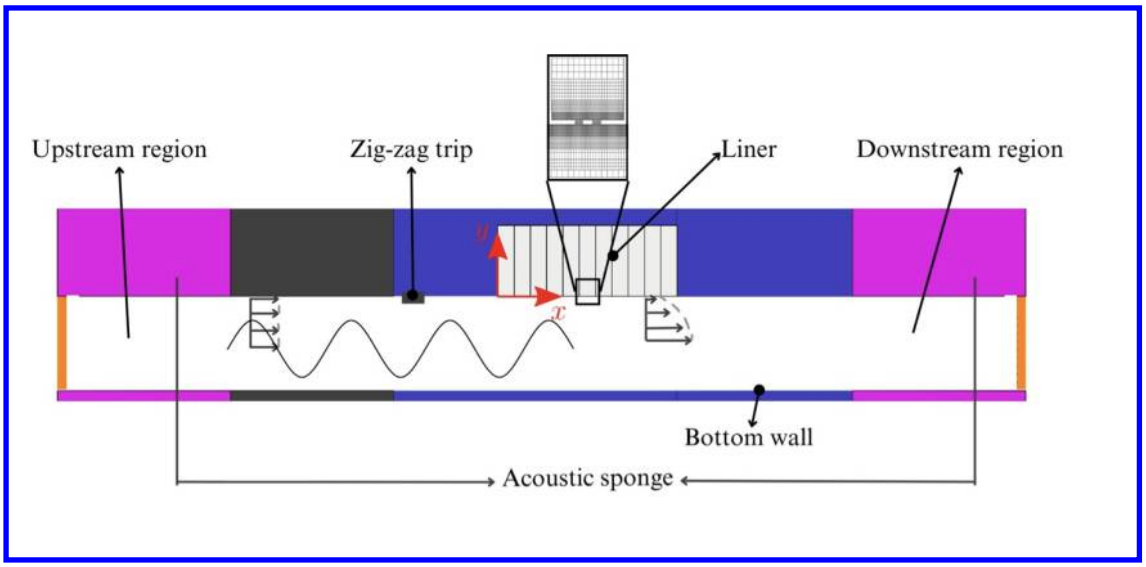

Fig. 3 Full computational domain.

Computations are conducted using a two-step approach: initially, the turbulent boundary layer within the duct is computed until convergence is reached. An instantaneous flow field is saved, which is then altered by overlaying a plane acoustic wave with specified frequency and amplitude using the *OptydB* toolkit. This modified flow field serves as the initial condition for high-fidelity numerical simulations with the added acoustic wave. This approach offers the advantage of reducing computational expenses, particularly when studying numerous different configurations.

The test matrix is summarized in Table 1; for each combination of SPL and frequency, acoustic sources propagating in the same direction and in the direction opposite to the mean flow one are also investigated. The Mach number at the centerline is equal to 0.32, as in the reference experiment. The SPL in the table has been calculated using the reference pressure of 20×10^{-6} Pa.

Surface data for estimating the impedance was sampled at 420 kHz. For each configuration, at least ten acoustic periods were considered for post-processing. Data was sampled after the unsteady field convergence.

Table 1 Test matrix.

$SPL[dB]$	$f[Hz]$	M
130	800, 1400, 2000	0.32
145	800, 1400, 2000	0.32

IV. Impedance Measurement Technique

A. In-Situ Technique

The in-situ technique, also known as the two-microphone method, was first proposed by Dean [40]. It involves measuring unsteady pressure at the face-sheet and at the bottom of the cavity. This method provides a point-wise measurement of impedance. It is based on the following key assumptions: the wavelength of the incident acoustic wave is significantly larger than the cavity width; the walls of the cavity are considered to be sufficiently thick, resulting in the liner being locally reactive (i.e., there is no transmission of energy across the wall [40]); any wave entering the cavity is assumed to be completely reflected at the backplate. As a consequence, the acoustic pressure of the standing wave within the cavity is the sum of the incident and reflected ones. Using the linearized momentum equation, it is possible to calculate the acoustic-induced velocity and, subsequently, the impedance as:

$$Z_f = \frac{Z}{Z_0} = -i\tilde{H}_{fb}\frac{1}{\sin(k\lambda)}; \tag{7}$$

where $\tilde{H}_{fb}$ is the transfer function defined as the ratio between the pressure measured at the face-sheet $\tilde{p}_f$ and at the backplate $\tilde{p}_b$, and $k = \omega/c_0$ is the free-field wavenumber, with ω being the acoustic wave angular frequency. This technique has been widely used for calculating the impedance of acoustic liners in the presence of grazing flow [13, 41]. As opposed to impedance eduction techniques [42], a model of the acoustic field is not required for the in-situ technique, hence boundary conditions to model the liner are unnecessary. However, some studies have underlined the sensitivity of this technique on the sampling position [15, 19]. The experimental results presented in the following were obtained using probes located in the third cavity nearest to the acoustic source [42], as depicted in Figure 4a. Data from the numerical simulations have been extracted at the same locations, which is shown in Figure 4b for comparison.

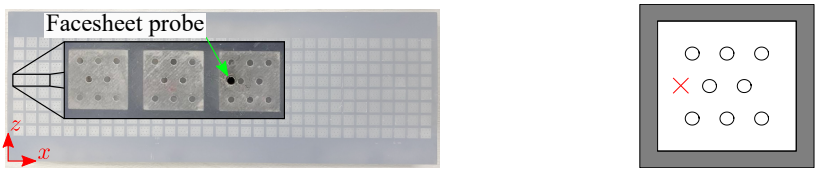

(a) **(b)**

Fig. 4 Position of the face-sheet probes for the assessment of the liner's impedance with the in-situ technique. (a) Experiments and (b) numerical simulations.

V. Preliminary Validation And Grid Convergence Study

The computational methodology is validated through grid convergence study and comparison against experimental data provided by Bonomo et al. [33] and Vallikivi et al. [43]. Validation is carried out to verify that both the integral turbulent boundary layer parameters and components of acoustic impedance match with the experiments.

A. Velocity profile

In both the experiments and numerical simulations, the TBL was evaluated upstream of the onset of the liner. Figure 5 depicts the velocity profiles obtained from the simulations without acoustic wave, carried out with three different resolutions, compared against experimental results obtained from hot-wire anemometry. In the plot, the spatial coordinate y is normalized by the channel height $H = 40$ mm. Experimental measurements are available only on the

half channel where the liner is placed. Small discrepancies exist between the bottom (i.e., opposite to where the liner is installed) and top wall (i.e., where the liner is installed) because of a slightly different discretization adopted to reduce the computational cost and the presence of a different pressure gradient, due to the presence of the liner in one side. The differences in the discretization between top and bottom walls explain why, for $y/H < 0.1$, the velocity profile has more data points. Overall, a good agreement between the experiments and simulation can be appreciated.

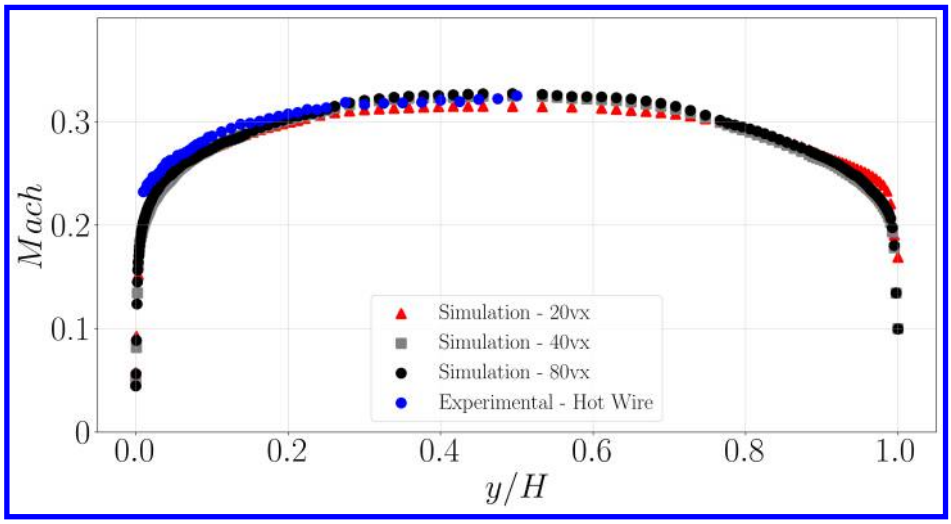

Fig. 5 Comparison of the experimental and numerical flow profile with different resolutions. The experimental flow profile is obtained with hot-wire anemometry.

Figure 6a shows the mean turbulent velocity profile. Inner boundary layer coordinates are used, i.e., $y^+ = yu_\tau/\nu$ and $u^+ = u/u_\tau$, where $u_\tau = \sqrt{\tau_w/\rho_w}$ is the friction velocity and τ_w is the wall shear stress. Experiments and simulations data, with resolution equal to 40 vx/d and 80 vx/d, are further compared with the law-of-the-wall with constants $k = 0.41$ and $B = 5.2$ [44]. For the sake of clarity, the turbulent boundary layer thickness has been calculated as δ_{99}, while u_τ from the experiments has been extrapolated through numerical fitting to the law of the wall [45]. Experimental findings, empirical model and results obtained from simulation with Fine resolution and Very Fine resolution show a noteworthy agreement.

Measurements of the stream-wise component of the Reynolds stresses are plotted in Figure 6b using simulation and experimental data [43]. Data from the literature is used because experimental velocity fluctuations were not available. The stream-wise component of the Reynolds stresses are normalized by u_τ and the density at the wall ρ_w. The amplitude of the peak for both simulations is close to 9, while its location is at $y^+ \approx 16$. Outside the viscous sublayer, the profiles show a Reynolds number dependence [46, 47]. Simulation data, at $Re_\tau = 3341$, are in good agreement with experimental results at a similar Re_τ [43].

To further validate the simulations, the amplitude and location of the peak of the stream-wise component of the Reynolds stresses are compared against the one obtained by applying the semi-empirical fit proposed by Klewicki et al. [48]:

$$u'^2_{max} = 8.5 \times 10^{-9} Re_\tau^2 + 4.8 \times 10^{-4} Re_\tau + 6.86; \tag{8}$$

$$y^+(u'^2) = 1.7 \times 10^{-4} Re_\tau + 14.4; \tag{9}$$

which yields $y^+(u'_{max}) \approx 15$ and non-dimensional $u'_{max} \approx 9$. This agreement confirms the reliability of the numerical model used in the study.

It is important to note that wiggles observed in Figure 6b in the outer layer are mainly related to an insufficient statistical convergence due to the limited data sample for a temporally growing boundary layer.

It is well known that the boundary layer turnover is an important parameter in the assessment of the flow statistical convergence [50], defined as Ut/δ. Converged statistics typically require several thousand events because the largest flow features can exceed 6δ in wavelength [46]. For this reason, results were considered after a boundary layer turnover time equal to 2000 times.

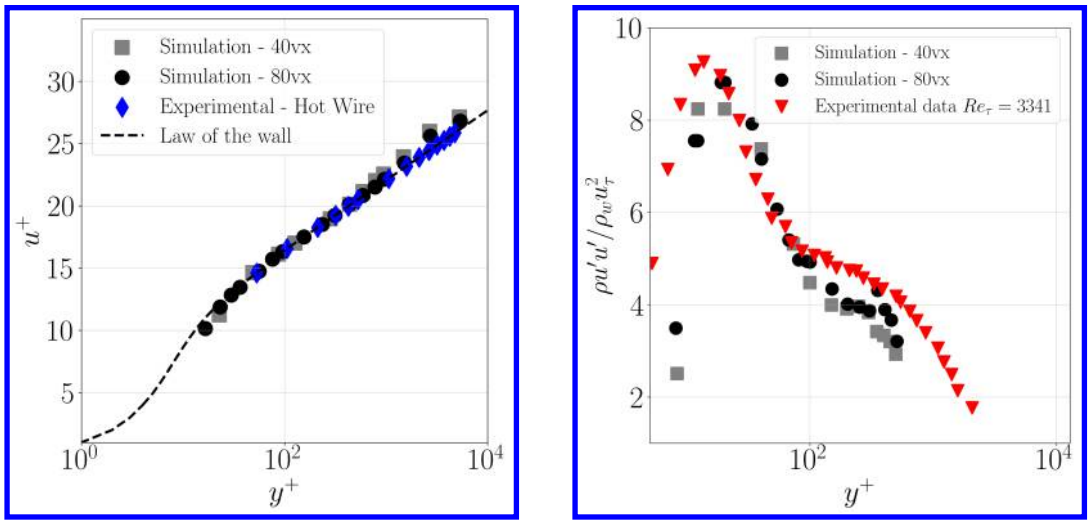

(a) **(b)**

Fig. 6 Comparisons of: (a) flow profiles with centerline Mach number equal to 0.32 with experimental data provided by Bonomo et al. [49]; (b) stream-wise component of the Reynolds stress with the experiments from Vallikivi et al. [43].

Figure 7 depicts the ratio of the numerical and experimental δ and u_τ as a function of the number of fine equivalent voxels. It is visible that computational data converges towards the experimental one as the resolution increases. The trends shown in the figure suggest that a resolution of 40 vx/d is sufficient to represent the flow within the duct.

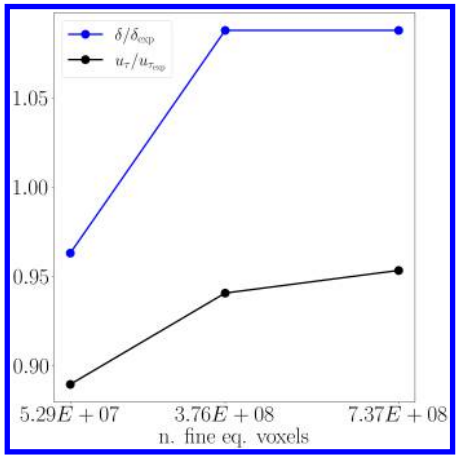

Fig. 7 Grid convergence study for the boundary layer thickness and the shear velocity.

B. Impedance

In Figure 8, impedance obtained from simulations and experiments [42] are compared. For the sake of conciseness, only the case with grazing flow at centerline Mach number equal to 0.32 and amplitude of the acoustic wave equal to 145 dB is considered, since it is the most challenging case given the non-linear effects. Furthermore, computational and experimental data are compared against the prediction from the semi-empirical model devised by Yu et al. [26], also known as the UTAS model, in the following. That model was selected because it accounts for a boundary layer parameter, i.e., the Boundary Layer Displacement Thickness (BLDT). Different mesh refinements, Medium and Fine (i.e., 20 vx/d and 40 vx/d), have been tested. Acoustic simulations were not performed at 80 vx/d because the boundary layer did not show any major variation with respect to the 40 vx/d case.

It is noted that simulations provide reasonable results with all refinement levels. Negligible changes are observed

moving from the medium resolution to the fine. This suggests that, for this specific case, the impact of the variation of the boundary layer properties with resolution has a minimum effect on impedance measured with the in-situ method. However, because of the grid resolution study shown above, data with a resolution of 40 vx/d are used for the following analyses.

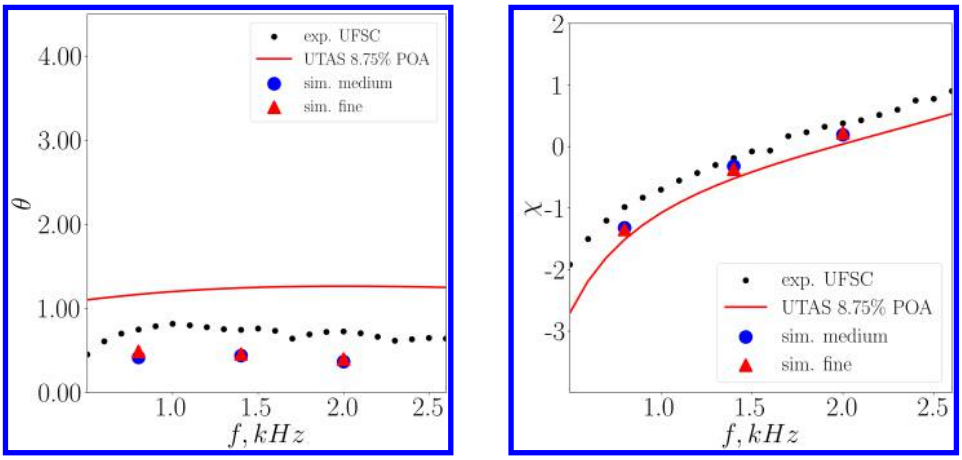

(a) **(b)**

Fig. 8 Mesh convergence analysis of (a) resistance and (b) reactance obtained from simulations at $M = 0.32$ and acoustic source with amplitude equal 145 dB, compared with experimental findings of Bonomo et al. [42] and prediction from the semi-empirical model proposed by Yu et al. [26]

Impedance values obtained from the numerical simulation agree well with experimental findings. In the presence of flow, the resistance is less dependent on the frequency and has a rather flat behaviour, which is related to the fact that the mean flow dominates the response of the liner. It is worth noting that the semi-empirical model tends to underestimate the reactance and overestimate the resistance.

The fact that the impedance predictions are in good agreement with experimental results suggests that the simulations are able to capture the relevant physical mechanisms.

VI. Acoustic Results

This section dives deeper into the influence of SPL and flow interactions on the impedance of the liner, to shed light on how liners behave when subjected acoustic waves with varying amplitude and frequency and in the presence of grazing flow.

A. On the effect of the Sound Pressure Level

Figure 9 presents both components of impedance obtained from simulations with a resolution of 40 vx/d, grazing flow and two SPLs, equal to 130 dB and 145 dB, compared with experimental findings. The symbols in Figure 9 are values computed using a virtual probe at the same location as in the experiments, while the bar shows the standard deviation calculated from the impedance values on the first cavity.

The comparison reveals similar trends between experiments and simulations. Specifically, resistance values do not vary significantly with frequency, as expected, and they are very similar for both amplitudes of the acoustic wave. This confirms that the non-linear effects caused by the flow are dominant in this case. Resistance values predicted by the semi-empirical models are higher than the experimental and computational ones, and show larger variation with SPL compared to the simulations and experimental data. Reactance values are also close for both amplitudes of the acoustic waves. Those obtained from the numerical simulations are similar to predictions from the semi-empirical model, while the experimental ones are slightly higher. The discrepancies between simulations and experiments can be due to the fact that the geometries of the liners are not exactly the same.

Numerical simulations allow for a very large amount of virtual probes; therefore, it is possible to assess the impact of the sampling position on measurements of the acoustic impedance [51, 52]. In this sense, impedance values along the liner surface have been obtained by sampling pressure on the entire face-sheet. On the other hand, a single virtual

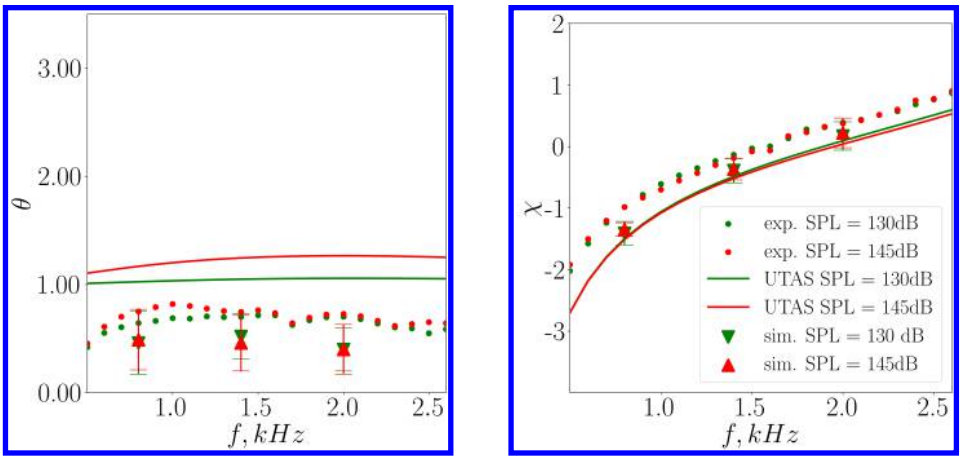

(a) **(b)**

Fig. 9 Comparison of (a) resistance and (b) reactance obtained from simulations at $M = 0.32$ and acoustic source equal to 130 and 145 dB, compared with experimental findings of Bonomo et al. [42] and prediction from semi-empirical model proposed by Yu et al. [26].

probe was considered at the backplate instead, at the center of each cavity. Results, for both components of impedance, considering SPL = 130 dB and 145 dB with a tonal excitation at $f = 1400$ Hz (i.e., near resonance frequency) are depicted in Figures 10 and 11. In these cases, the flow and acoustic waves propagate from the left to the right. The figures illustrate how the measured component varies from the surface-averaged mean value, emphasizing the importance of probe location. For the case at SPL = 130 dB, $\theta_{\text{mean}} = 0.775$ and $\chi_{\text{mean}} = -0.522$, while for the 145 dB case $\theta_{\text{mean}} = 0.798$ and $\chi_{\text{mean}} = -0.470$.

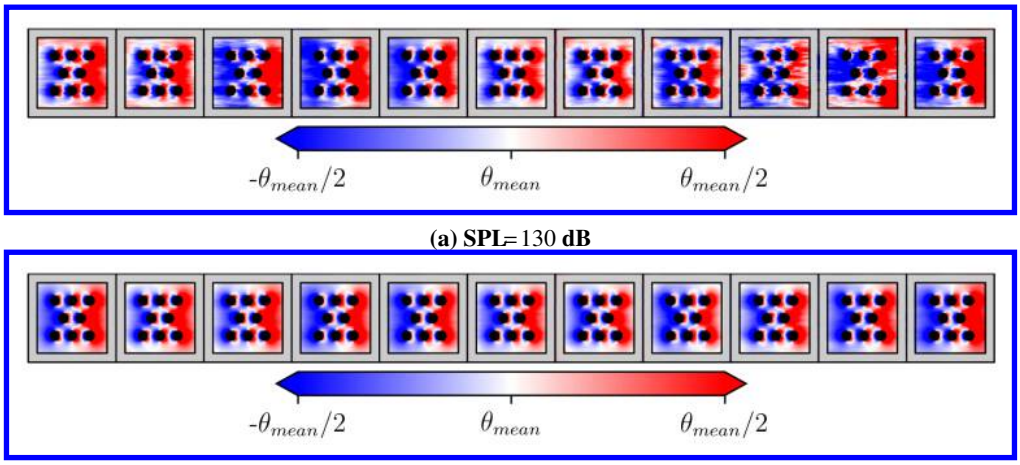

(a) SPL= 130 dB

(b) SPL= 145 dB

Fig. 10 Resistance along liner's surface calculated through in-situ method as a function of SPL, $f = 1400$ Hz with grazing flow with centerline Mach number equal to 0.32.

The case considering acoustic wave with SPL equal to 130 dB exhibits a less smooth variation along each cell, compared to the simulation with SPL equal to 145 dB. This is likely related to the lower signal-to-noise ratio for the former case. However, a similar trend can be observed for both SPL levels, resistance increases when moving from the left-hand side to the right-hand side of each cavity. Within each cavity, the resistance increases by a factor of three with local minimum near the upstream orifices and a local maximum near the downstream ones. Furthermore,

local peaks are found upstream and downstream of each orifice that can be related to the near-orifices vortices [51]. A similar behaviour, but with opposite trend, is present for the reactance values. It is found that, the peak of resistance is observed downstream the orifice near the right-hand termination of each cavity, in the same place where the minimum of reactance is located.

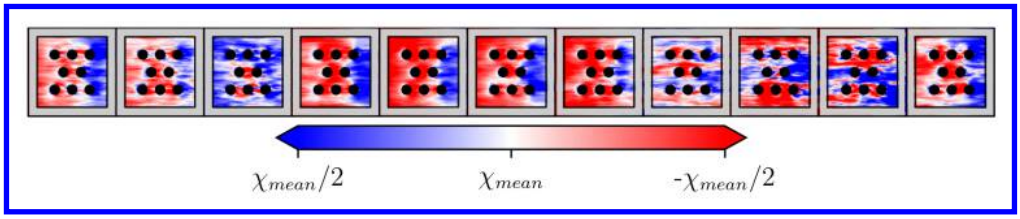

(a) SPL= 130 dB

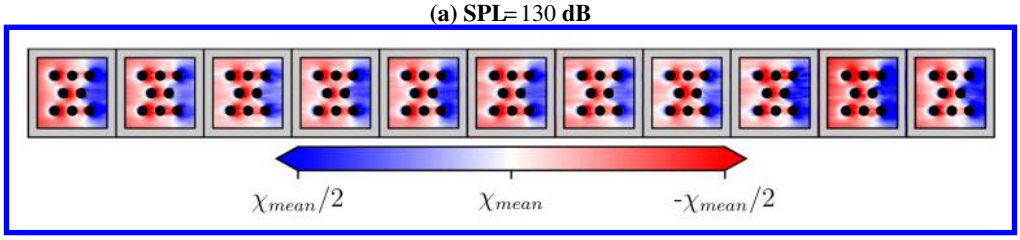

(b) SPL= 145 dB

Fig. 11 Reactance along liner's surface calculated through in-situ method as a function of SPL, $f = 1400$ Hz with grazing flow with centerline Mach number equal to 0.32.

It is observed a slight increase of the average reactance and a decrease of the average resistance from the most upstream to the most downstream cavity. This is related to the reduction of the SPL of the grazing acoustic wave along the liner, as shown in Figure 12. In the figure, data from both experiments and simulations are shown. In this case, the experimental data are obtained for the same number of cavities as considered in the simulations. For the sake of comparison, the SPL is normalized with respect to the SPL at the beginning of the liner, named SPL_{max}. It is worth noticing that the SPL decay obtained from simulations is slightly overestimated on the last two cavities probably due to acoustic scattering caused by the change of impedance from liner to solid wall. However, simulations and measurements show good agreement and a similar slope for the most upstream cavities.

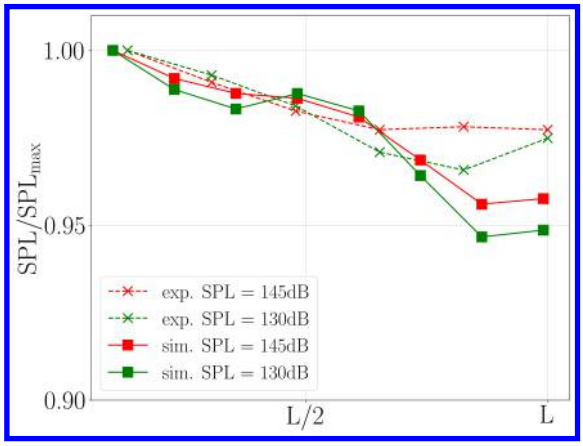

Fig. 12 SPL decay obtained from experiments and simulations with grazing flow, different SPLs and $f = 1400Hz$, calculated at the middle of the channel.

In order to further verify that the variations along the liner found in the simulations are reliable, experiments were conducted with two probes located upstream and downstream of the third cavity. Figure 13 illustrates the impedance

obtained at two distinct positions for the case with grazing acoustic wave with SPL equal to 145 dB. The comparison between experiments and simulations confirms what was previously stated and that there is an increase in resistance up to a factor of three and a decrease in reactance independent of the frequency of the acoustic excitation. These findings are in agreement with the observations made by Hersh and Walker [21], highlighting the substantial influence of mean flow and the interaction between acoustics and flow within the orifice and its face-sheet, thereby influencing impedance locally. The variations along each cavity and near the orifices can be attributed to the presence of near-wake orifices that can enhance velocity and pressure fluctuations at the face-sheet.

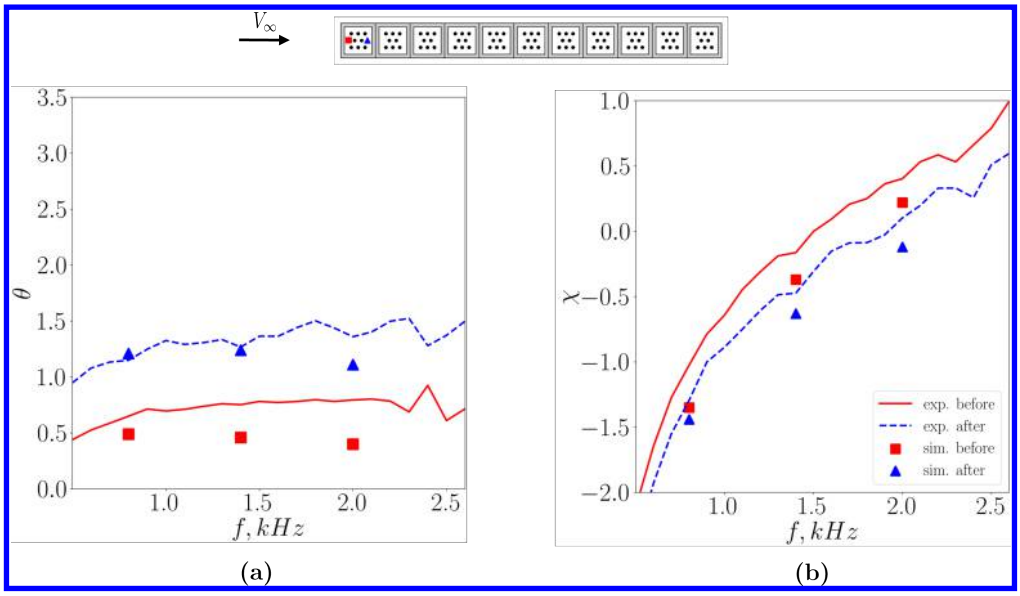

Fig. 13 Comparison of the (a) resistance and (b) reactance obtained from simulations at $M = 0.32$ and acoustic source with amplitude equal to 145 dB, in different positions along the liner's surface, with experimental findings [28].

To provide further evidence that the near wake of the most upstream orifice affects the downstream one, the flow within the cavity is analysed. Specifically, the acoustic-induced velocity within the orifice is obtained using a triple decomposition approach [13, 15]. Figure 14 shows the spatial distribution of the phase-locked acoustic-induced velocity along the centerline of two adjacent orifices at a wall-normal location equal to $y = \tau/2$. The acoustic-induced velocity is presented in a dimensionless form, normalized by u_τ. Results corresponding to two phase angles are shown: $\phi = 0°$ and 180°; where $\phi = 0°$ is defined as the peak of pressure in the inflow phase at the orifice considered.

Results agree with the findings of Léon et al. [53] and Zhang and Bodony [13]. As the sound pressure levels increase, the acoustic-induced velocity within the cavity grows. Furthermore, as observed in previous works, a spatial asymmetry exists between the upstream and downstream edge of each orifice due to the presence of a quasi-steady vortex. Differences between the inflow and outflow phases are also found. This appears to be more relevant for the downstream orifice, and it might be caused by the near-orifice vorticity shed from the upstream orifice advected downstream. It can be observed that both the inflow and outflow velocity profiles show a peak in the downstream half of the orifice. This is likely related to the effect of the reduced area for flow passage due to the presence of grazing flow [21]. The figure highlights, the role of the quasi-steady vortex within the cavity, that obstructs the periodic flow-induced motion caused by the acoustic wave. In this case, differently from previous studies [19], it is possible to observe that velocity fluctuations are still present after phase averaging. This is likely due to the thinner face-sheet thickness and rounding of the orifices that favourite the turbulent velocity fluctuations to penetrate within the orifices.

It is important to note that the velocity profiles in the first and second orifice differ. This indicates that the wake of the first orifice affects the flow entering the second one. The second orifice has a larger inflow area and higher maximum velocity when compared to the first one. This difference can be clearly seen in Figure 15, which shows the contour plots of the acoustic-induced velocity for two different SPLs at the frequency of $f = 1400$ Hz. The increase in the acoustic-induced velocity with increasing the SPL is confirmed, and it is worth noting that the inflow areas are different.

One can assume that the varying velocity distribution across the hole diameter of the first and second orifice implies

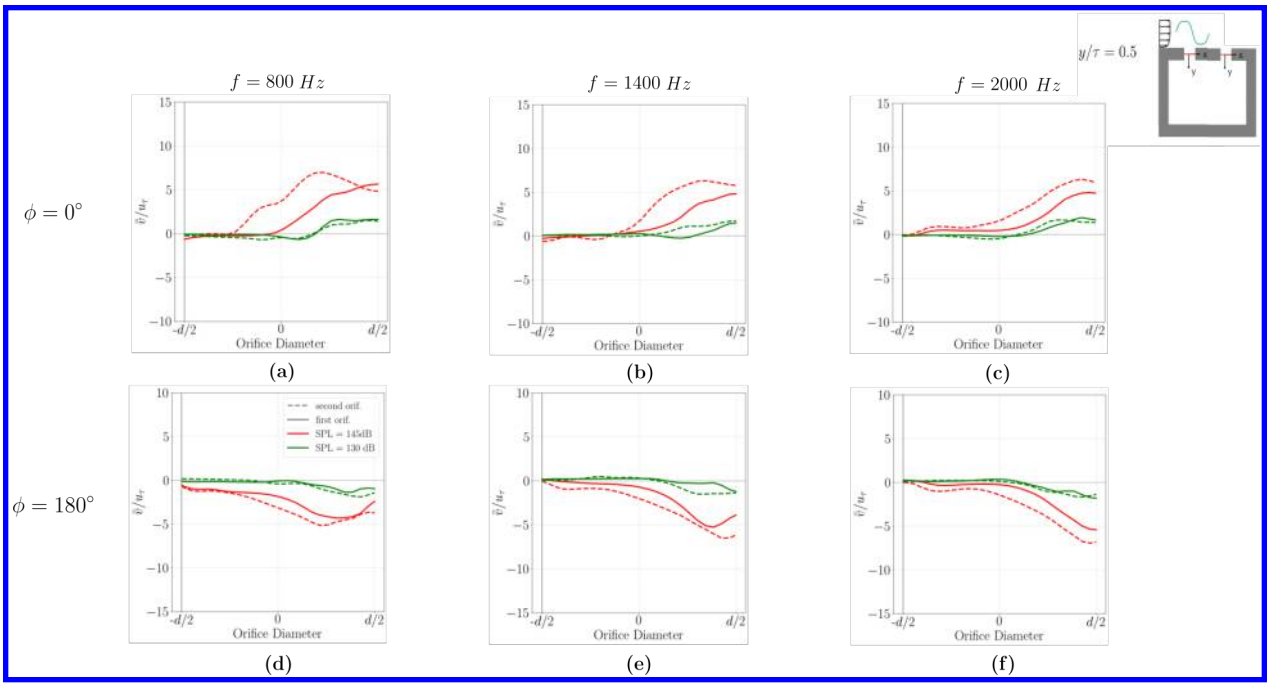

Fig. 14 Spatial distribution along the diameter of the acoustic-induced vertical velocity $\bar{\bar{v}}$ as a function of the SPL: (a, c) $\phi = 0°$; (d, f) $\phi = 180°$. Acoustic wave with SPL equal to 130dB and 145 dB.

the presence of vorticity advected downstream from the first orifice, which affects the flow entering the second orifice. Thus, while modelling the acoustic response of the liner, it is crucial to consider the flow within the orifice, as it is a major factor.

B. On the effect of the acoustic source position with respect to the mean flow

This section investigates the effect of the direction of acoustic wave propagation with respect to the mean flow. Figures 16 and 17 present results for acoustic waves with amplitudes equal to 130 dB and 145 dB, respectively, considering two different directions of propagation at frequencies of 800 Hz, 1400 Hz, and 2000 Hz. Nomenclature (upstream) refers to upstream acoustic source, thus downstream propagation, while (downstream) refers to downstream source, thus upstream propagation. Impedance has been calculated with Dean's method [40]. The symbols and bars are as above.

Both the experimental and numerical results depend on the acoustic wave direction of propagation. The resistance increases by a factor of two when the acoustic wave propagates in the direction opposite to the mean flow, while the reactance is less affected by this factor. The standard deviation increases for the downstream case as well. Similar results have been extensively documented in literature [33, 54] and contradict the assumption of locally reacting liner.

The differences in resistance between the two directions can be due to different physical mechanisms. On the aerodynamic side, a different boundary layer, due to the periodic motion induced by the acoustic wave, can heavily affect the flow within the orifice, thus affecting the effective percentage of open area and changing the liner's acoustic response. From the acoustic perspective, boundary layer refraction can affect the measured impedance differently for the two directions of propagation, as reported by Spillere et al. [54].

Therefore, to distinguish if the differences are mainly of aerodynamics or acoustic nature, the acoustic-induced velocity has been calculated. Contours plot of the acoustic-induced velocities are shown in Figure 18, for the case with acoustic wave with amplitude equal to 145 dB and frequency equal to 1400 Hz. The cavity closest to the acoustic source is considered for each case, i.e., that in which the SPL is higher. Figures on the left depict the first cavity (most upstream position) relative to the flow direction, whereas those on the right illustrate the most downstream cavity. A notable disparity between the two cases is evident in the figures. The orifice area in which a periodic motion is visible is larger for the downstream case than for the upstream one. This result is unexpected because a different trend can be expected looking at the resistance component of impedance. The reasons for this behaviour will be further investigated in the

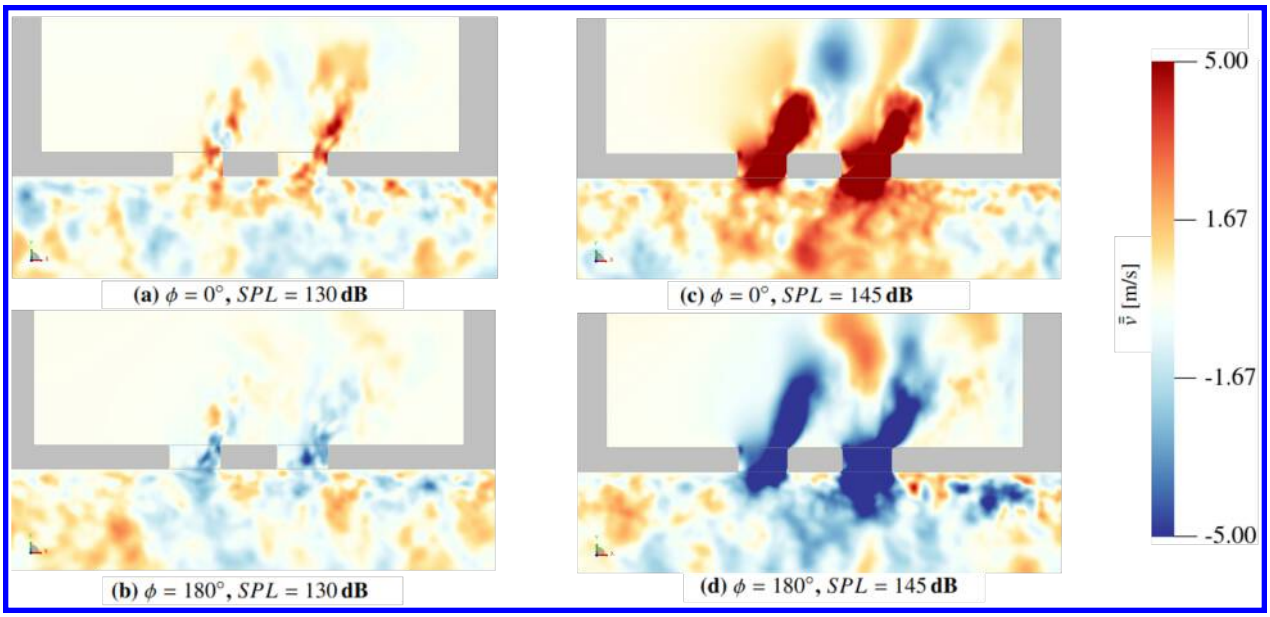

Fig. 15 Contour plot of acoustic-induced vertical velocity $\bar{\tilde{v}}$ for two different SPLs and $f = 1400Hz$.

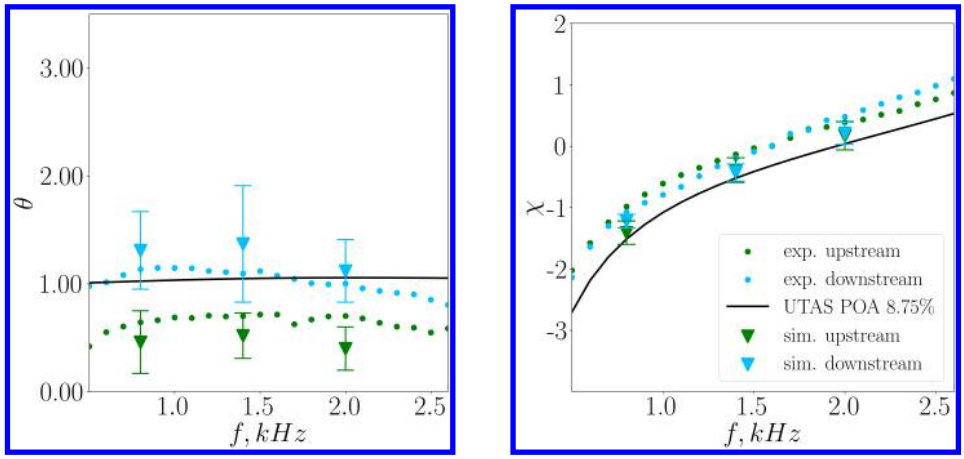

(a) **(b)**

Fig. 16 Dependence of the (a) resistance and (b) reactance component of impedance on the relative direction of propagation between the free-stream velocity and the acoustic wave for SPL = 130 **dB.**

future. It is evident that in the upstream case, the acoustic wave penetrates deeper into the cavity.

The acoustic-induced velocity is then extracted at the center of the orifice and shown in Figure 19. The figures clearly show that the maximum acoustic-induced velocity between the two cases is very similar but differences are mainly due to their spatial distribution. Furthermore, a symmetric behaviour is found between inflow and outflow thus suggesting that the changes in impedance between the upstream and downstream case are mainly due to the effective open area.

VII. Conclusions

Simulations of a multi-orifice acoustic liner, subjected to a turbulent flow with centerline Mach number equal to 0.32 and planar acoustic wave with amplitudes of 130 dB and 145 dB and frequencies of 800, 1400, and 2000 Hz, were conducted using lattice-Boltzmann Very Large Eddy simulations. The simulations replicated the experiments carried out in the liner facility at UFSC, which were used as a reference for comparison. The simulations were carried out in two steps: the turbulent flow over the acoustic liner was computed until convergence was reached, and then a planar

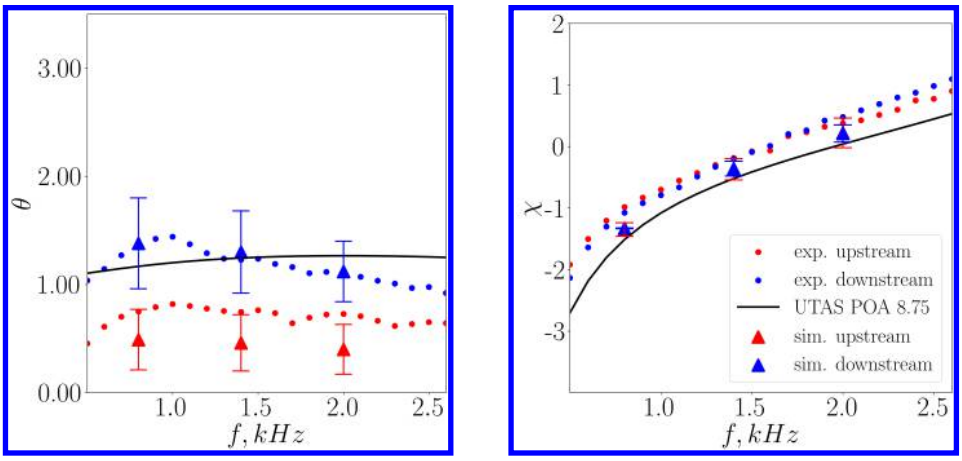

(a) **(b)**

Fig. 17 Dependence of the (a) resistance and (b) reactance component of impedance on the relative direction of propagation between the free-stream velocity and the acoustic wave for SPL = 145 **dB.**

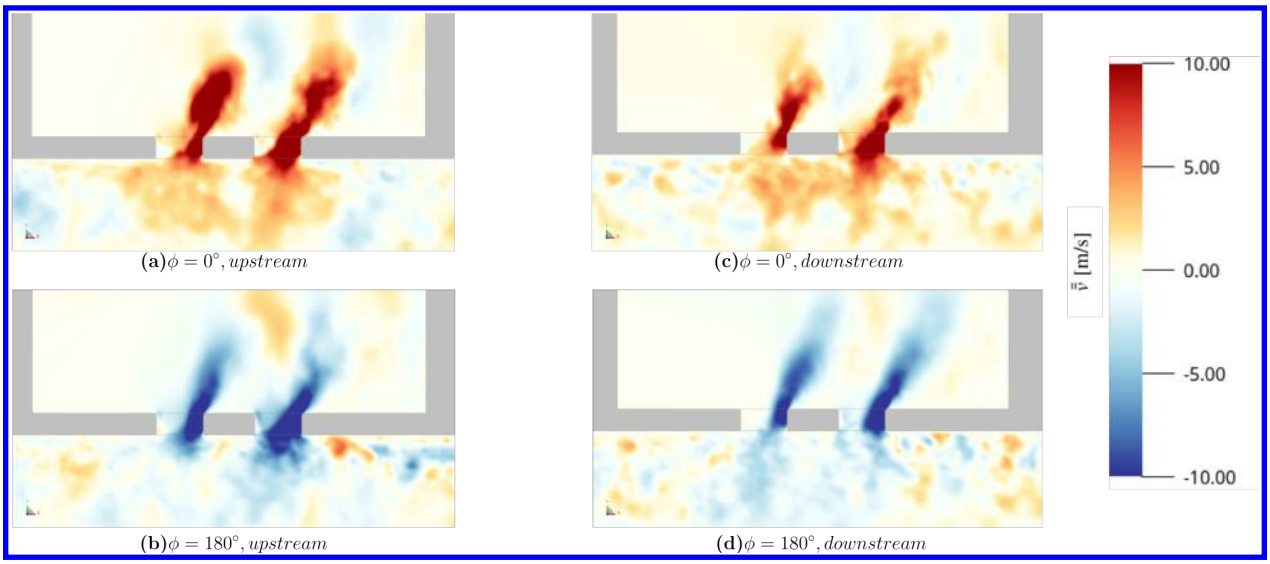

Fig. 18 Contour plot of acoustic-induced vertical velocity $\bar{\bar{v}}$ for SPL equal to 145 dB, $f = 1400$ Hz and different acoustic source directions with respect to the grazing flow.

acoustic wave was superimposed using the *OptydB* toolkit.

The time-averaged turbulent boundary layer was compared with experimental reference data from Bonomo et al. [42] and Vallikivi et al. [43], and good agreement was found. Furthermore, simulations were further validated by comparing both components of the acoustic impedance, calculated with the Dean's method, against experiments [42]. Results show that the resistance does not vary significantly with SPL and frequency when there is grazing turbulent flow. This confirms that the presence of turbulent flow dominates the acoustic response of the liner. Furthermore, consistent differences were found when comparing acoustic sources propagating in the same direction and in the direction opposite to the mean flow, for both experiments and simulations.

The acoustic-induced velocity in the near-orifice regions was computed using a triple decomposition approach. Results support the conclusion that the grazing flow heavily affects the acoustic response of the liner. This is mainly because a quasi-steady vortex forms within the orifice, reducing the effective open area. The quasi-steady vortex affects the penetration of the acoustic wave in a different way depending on the relative direction of propagation of the acoustic wave. Furthermore, when comparing two orifices, one downstream of the other, it is evident that there is an impact of

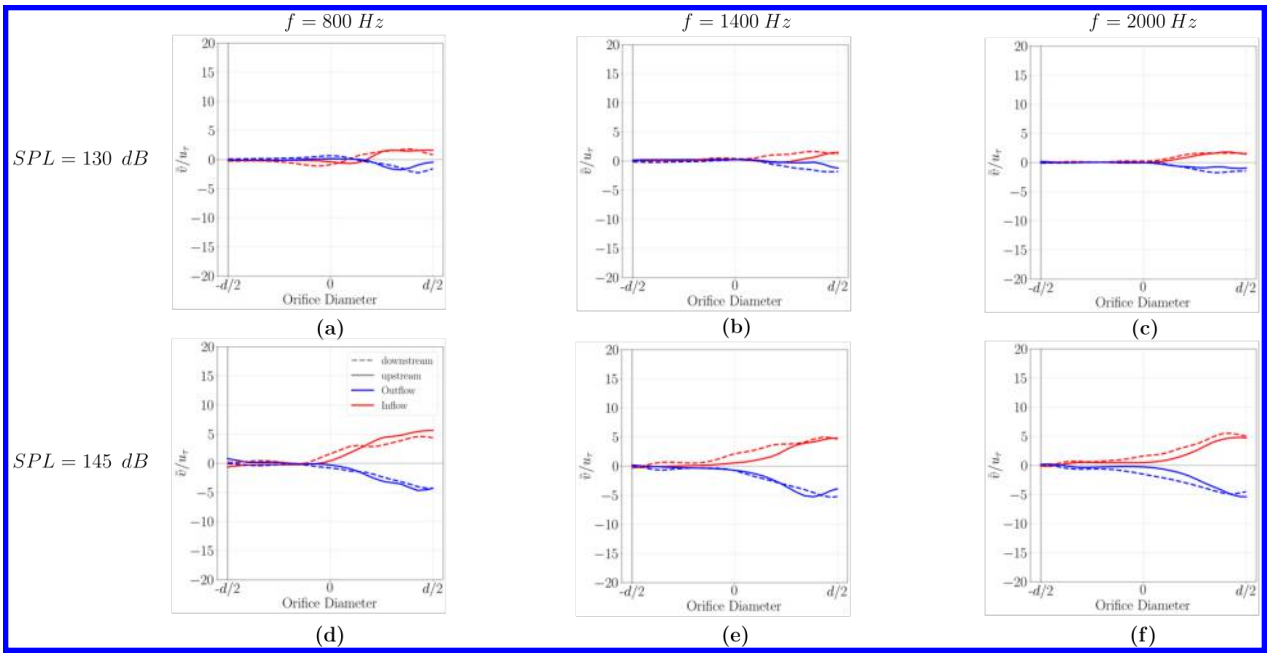

Fig. 19 Spatial distribution along the diameter of the acoustic-induced vertical velocity $\bar{\bar{v}}$ with a SPL equal to 130 dB (top row) and 145 dB (bottom row) and two different acoustic source positions with respect to the grazing flow.

the near wake flow shed by the most upstream orifice to the downstream one, thus affecting the velocity distribution and amplitude.

VIII. Acknowledgments

The work of A. Paduano and F. Avallone is co-funded by the European Union (ERC, LINING, 101075903). Views and opinions expressed are however those of the author(s) only and do not necessarily reflect those of the European Union or the European Research Council. Neither the European Union nor the granting authority can be held responsible for them. This work was partially supported by the AeroAcoustics Research Consortium (AARC). The AARC is a government-industry partnership supporting pre-competitive research for aircraft noise reduction. L.A. Bonomo, L.M. Pereira and J.A. Cordioli gratefully acknowledge funding from Conselho Nacional de Desenvolvimento Científico e Tecnológico (CNPq), project number 407583/2022-0. On behalf of L.A. Bonomo, this study was financed in part by the Coordenação de Aperfeiçoamento de Pessoal de Nível Superior – Brasil (CAPES) – Finance Code 001. L.M. Pereira acknowledges scholarship funding from CNPq. L.A. Bonomo also acknowledges CNPq scholarship number 402701/2022-4

References

[1] Mallat, S., "A theory for multiresolution signal decomposition: the wavelet representation," *IEEE Transactions on Pattern Analysis and Machine Intelligence*, Vol. 11, No. 7, 1989, pp. 674–693. https://doi.org/10.1109/34.192463.

[2] Hughes, C., "The Promise and Challenges of Ultra High Bypass Ratio Engine Technology and Integration," *AIAA Aero Sciences Meeting*, 2011, pp. 0–11. URL https://ntrs.nasa.gov/citations/20110011737.

[3] Casalino, D., Hazir, A., and Mann, A., "Turbofan broadband noise prediction using the lattice boltzmann method," *AIAA Journal*, Vol. 56, No. 2, 2018. https://doi.org/10.2514/1.J055674.

[4] Motsinger, R. E., and Kraft, R. E., "Design and performance of duct acoustic treatment," *NASA. Langley Research Center, Aeroacoustics of Flight Vehicles: Theory and Practice. Volume 2: Noise Control*, 1991. URL https://ntrs.nasa.gov/citations/19920005565.

[5] Anselmet, F., and Mattei, P., *Acoustics, Aeroacoustics and Vibrations*, 1st ed., Wiley, 2016. https://doi.org/10.1002/9781119178361.

[6] Rienstra, S. W., and Hirschberg, A., *An introduction to acoustics*, Technische Universiteit Eindhoven, 2004.

[7] Jones, M. G., Tracy, M. B., Watson, W. R., and Parrott, T. L., "Effects of liner geometry on acoustic impedance," *8th AIAA/CEAS Aeroacoustics Conference and Exhibit*, American Institute of Aeronautics and Astronautics Inc., 2002. https://doi.org/10.2514/6.2002-2446.

[8] Brokof, P., Guzmán-Iñigo, J., Yang, D., and Morgans, A. S., "The acoustics of short circular holes with reattached bias flow," *Journal of Sound and Vibration*, Vol. 546, 2023. https://doi.org/10.1016/j.jsv.2022.117435.

[9] Temiz, M. A., Lopez Arteaga, I., Efraimsson, G., Åbom, M., and Hirschberg, A., "The influence of edge geometry on end-correction coefficients in micro perforated plates," *The Journal of the Acoustical Society of America*, Vol. 138, No. 6, 2015, pp. 3668–3677. https://doi.org/10.1121/1.4937748.

[10] Melling, T., "The acoustic impendance of perforates at medium and high sound pressure levels," *Journal of Sound and Vibration*, Vol. 29, No. 1, 1973, pp. 1–65. https://doi.org/10.1016/S0022-460X(73)80125-7.

[11] Tam, C. K., and Kurbatskii, K. A., "Microfluid dynamics and acoustics of resonant liners," *AIAA journal*, Vol. 38, No. 8, 2000, pp. 1331–1339. https://doi.org/10.2514/2.1132.

[12] Murray, P. B., and Jeremy Astley, R., "Development of a single degree of freedom perforate impedance model under grazing flow and high SPL," *18th AIAA/CEAS Aeroacoustics Conference (33rd AIAA Aeroacoustics Conference)*, 2012. https://doi.org/10.2514/6.2012-2294.

[13] Zhang, Q., and Bodony, D. J., "Numerical investigation of a honeycomb liner grazed by laminar and turbulent boundary layers," *Journal of Fluid Mechanics*, Vol. 792, 2016, pp. 936–980. https://doi.org/10.1017/jfm.2016.79.

[14] Kooijman, G., Hirschberg, A., and Golliard, J., "Acoustical response of orifices under grazing flow: Effect of boundary layer profile and edge geometry," *Journal of Sound and Vibration*, Vol. 315, No. 4-5, 2008, pp. 849–874. https://doi.org/10.1016/j.jsv.2008.02.030.

[15] Avallone, F., and Casalino, D., "Acoustic-induced velocity in a multi-orifice acoustic liner grazed by a turbulent boundary layer," *AIAA Aviation and Aeronautics Forum and Exposition, AIAA AVIATION Forum 2021*, American Institute of Aeronautics and Astronautics Inc, AIAA, 2021. https://doi.org/10.2514/6.2021-2169.

[16] Ingard, U., "Influence of Fluid Motion Past a Plane Boundary on Sound Reflection, Absorption, and Transmission," *The Journal of the Acoustical Society of America*, Vol. 31, No. 7, 1959, pp. 1035–1036. https://doi.org/10.1121/1.1907805.

[17] Myers, M. K., "On the acoustic boundary condition in the presence of flow," *Journal of Sound and Vibration*, Vol. 71, No. 3, 1980. https://doi.org/10.1016/0022-460X(80)90424-1.

[18] Aurégan, Y., Starobinski, R., and Pagneux, V., "Influence of grazing flow and dissipation effects on the acoustic boundary conditions at a lined wall," *The Journal of the Acoustical Society of America*, Vol. 109, No. 1, 2001. https://doi.org/10.1121/1.1331678.

[19] Pereira, L. M., Bonomo, L. A., Quintino, N. T., da Silva, A. R., Cordioli, J. A., and Avallone, F., "Validation of High-Fidelity Numerical Simulations of Acoustic Liners Under Grazing Flow," *AIAA AVIATION 2023 Forum*, 2023. https://doi.org/10.2514/6.2023-3503.

[20] Baumeister, K. J., and Rice, E. J., "Visual study of the effect of grazing flow on the oscillatory flow in a resonator orifice," , 1975.

[21] Hersh, A. S., and Walker, B., "Effect of grazing flow on the acoustic impedance of Helmholtz resonators consisting of single and clustered orifices." , 1979. https://doi.org/10.2514/6.1978-1124.

[22] Zhang, Q., and Bodony, D. J., "Numerical simulation of two-dimensional acoustic liners with high-speed grazing flow," *AIAA Journal*, Vol. 49, No. 2, 2011, pp. 365–382. https://doi.org/10.2514/1.J050597.

[23] Jones, M. G., and Watson, W. R., "On the use of experimental methods to improve confidence in educed impedance," *17th AIAA/CEAS Aeroacoustics Conference 2011 (32nd AIAA Aeroacoustics Conference)*, 2011. https://doi.org/10.2514/6.2011-2865.

[24] Howe, M. S., "Emendation of the Brown & Michael equation, with application to sound generation by vortex motion near a half-plane," *Journal of Fluid Mechanics*, Vol. 329, 1996. https://doi.org/10.1017/S002211209600883X.

[25] Cummings, A., "The response of a resonator under a turbulent boundary layer to a high amplitude non-harmonic sound field," *Journal of Sound and Vibration*, Vol. 115, No. 2, 1987. https://doi.org/10.1016/0022-460X(87)90475-5.

[26] Yu, J., Ruiz, M., and Kwan, H. W., "Validation of Goodrich perforate liner impedance model using NASA langley test data," *14th AIAA/CEAS Aeroacoustics Conference (29th AIAA Aeroacoustics Conference)*, 2008. https://doi.org/10.2514/6.2008-2930.

[27] Schroeder, L., Spillere, A. M., Bonomo, L. A., da Silva, A. R., Cordioli, J. A., and Avallone, F., "Numerical Investigation of Acoustic Liners Experimental Techniques using a Lattice-Boltzmann Solver," *AIAA Aviation and Aeronautics Forum and Exposition, AIAA AVIATION Forum 2021*, 2021. https://doi.org/10.2514/6.2021-2144.

[28] Pereira, L. M., "High-Fidelity Numerical Simulations of Acoustic Liners Under Grazing Flow," Master thesis in mechanical engineering, Universidade Federal de Santa Catarina, Florianópolis, 2023. https://doi.org/10.13140/RG.2.2.12789.38882.

[29] Mann, A., Pérot, F., Kim, M. S., and Casalino, D., "Characterization of acoustic liners absorption using a lattice-Boltzmann method," *19th AIAA/CEAS Aeroacoustics Conference*, 2013. https://doi.org/10.2514/6.2013-2271.

[30] Hazir, A., and Casalino, D., "Effect of temperature variations on the acoustic properties of engine liners," *23rd AIAA/CEAS Aeroacoustics Conference, 2017*, 2017. https://doi.org/10.2514/6.2017-3874.

[31] Rego, L., Avallone, F., Ragni, D., Casalino, D., and Denayer, H., "Acoustic liners for jet-installation noise reduction," *Journal of Sound and Vibration*, Vol. 537, 2022. https://doi.org/10.1016/j.jsv.2022.117189.

[32] Cerizza, D., and Casalino, D., "An Indirect Impedance Eduction Process for Liners with Arbitrarily Complex Geometry," 2023. https://doi.org/10.2514/6.2023-4186.

[33] Bonomo, L. A., Quintino, N. T., Cordioli, J. A., Avallone, F., Jones, M. G., Howerton, B. M., and Nark, D. M., "A Comparison of Impedance Eduction Test Rigs with Different Flow Profiles," *AIAA AVIATION 2023 Forum*, 2023. https://doi.org/10.2514/6.2023-3346.

[34] He, X., and Luo, L. S., "Theory of the lattice Boltzmann method: From the Boltzmann equation to the lattice Boltzmann equation," *Physical Review E - Statistical Physics, Plasmas, Fluids, and Related Interdisciplinary Topics*, Vol. 55, No. 6, 1997. https://doi.org/10.1103/PhysRevE.56.6811.

[35] Bhatnagar, P. L., Gross, E. P., and Krook, M., "A model for collision processes in gases. I. Small amplitude processes in charged and neutral one-component systems," *Physical Review*, Vol. 94, No. 3, 1954. https://doi.org/10.1103/PhysRev.94.511.

[36] Qian, Y. H., D'Humières, D., and Lallemand, P., "Lattice bgk models for navier-stokes equation," *EPL*, Vol. 17, No. 6, 1992. https://doi.org/10.1209/0295-5075/17/6/001.

[37] Yakhot, V., and Orszag, S. A., "Renormalization-group analysis of turbulence," *Physical Review Letters*, Vol. 57, No. 14, 1986. https://doi.org/10.1103/PhysRevLett.57.1722.

[38] Teixeira, C. M., "Incorporating turbulence models into the Lattice-boltzmann method," *International Journal of Modern Physics C*, Vol. 9, No. 8, 1998. https://doi.org/10.1142/s0129183198001060.

[39] Launder, B. E., and Spalding, D. B., "The numerical computation of turbulent flows," *Computer Methods in Applied Mechanics and Engineering*, Vol. 3, No. 2, 1974. https://doi.org/10.1016/0045-7825(74)90029-2.

[40] Dean, P., "An in situ method of wall acoustic impedance measurement in flow ducts," *Journal of Sound and Vibration*, Vol. 34, No. 1, 1974, pp. 97–IN6. https://doi.org/https://doi.org/10.1016/S0022-460X(74)80357-3.

[41] Schuster, B., "A comparison of ensemble averaging methods using Dean's method for in-situ impedance measurements," *18th AIAA/CEAS Aeroacoustics Conference (33rd AIAA Aeroacoustics Conference)*, 2012. https://doi.org/10.2514/6.2012-2244.

[42] Bonomo, L. A., Quintino, N. T., Spillere, A. M., Cordioli, J. A., and Murray, P. B., "A Comparison of In-Situ and Impedance Eduction Experimental Techniques for Acoustic Liners with Grazing Flow and High SPL," *28th AIAA/CEAS Aeroacoustics Conference, 2022*, 2022. https://doi.org/10.2514/6.2022-2998.

[43] Vallikivi, M., Hultmark, M., and Smits, A. J., "Turbulent boundary layer statistics at very high Reynolds number," *Journal of Fluid Mechanics*, Vol. 779, 2015. https://doi.org/10.1017/jfm.2015.273.

[44] Coles, D., "The law of the wake in the turbulent boundary layer," *Journal of Fluid Mechanics*, Vol. 1, No. 2, 1956. https://doi.org/10.1017/S0022112056000135.

[45] Clauser, F. H., "Turbulent Boundary Layers in Adverse Pressure Gradients," *Journal of the Aeronautical Sciences*, Vol. 21, No. 2, 1954. https://doi.org/10.2514/8.2938.

[46] Hutchins, N., and Marusic, I., "Large-scale influences in near-wall turbulence," *Philosophical Transactions of the Royal Society A: Mathematical, Physical and Engineering Sciences*, Vol. 365, No. 1852, 2007. https://doi.org/10.1098/rsta.2006.1942.

[47] Wei, T., and Willmarth, W. W., "Reynolds-number effects on the structure of a turbulent channel flow," *Journal of Fluid Mechanics*, Vol. 204, No. 57, 1989. https://doi.org/10.1017/S0022112089001667.

[48] Klewicki, J. C., Murray, J. A., and Falco, R. E., "Vortical motion contributions to stress transport in turbulent boundary layers," *Physics of Fluids*, Vol. 6, No. 1, 1994. https://doi.org/10.1063/1.868082.

[49] Bouman, G., "Aero-acoustic response of an acoustic liner," Master thesis in aerospace engineering, Delft University of Technology, 2021. URL http://resolver.tudelft.nl/uuid:d0b525a2-ca09-4bfc-a8e3-7917d8099fc0.

[50] Monty, J. P., Harun, Z., and Marusic, I., "A parametric study of adverse pressure gradient turbulent boundary layers," *International Journal of Heat and Fluid Flow*, Vol. 32, No. 3, 2011. https://doi.org/10.1016/j.ijheatfluidflow.2011.03.004.

[51] Avallone, F., Manjunath, P., Ragni, D., and Casalino, D., "Lattice-boltzmann very large eddy simulation of a multi-orifice acoustic liner with turbulent grazing flow," *25th AIAA/CEAS Aeroacoustics Conference, 2019*, 2019. https://doi.org/10.2514/6.2019-2542.

[52] Manjunath, P., Avallone, F., Casalino, D., Ragni, D., and Snellen, M., "Characterization of liners using a lattice-boltzmann solver," *2018 AIAA/CEAS Aeroacoustics Conference*, 2018. https://doi.org/10.2514/6.2018-4192.

[53] Léon, O., Méry, F., Piot, E., and Conte, C., "Near-wall aerodynamic response of an acoustic liner to harmonic excitation with grazing flow," *Experiments in Fluids*, Vol. 60, No. 9, 2019. https://doi.org/10.1007/s00348-019-2791-5.

[54] Spillere, A. M. N., Bonomo, L. A., Cordioli, J. A., and Brambley, E. J., "Experimentally testing impedance boundary conditions for acoustic liners with flow: Beyond upstream and downstream," *Journal of Sound and Vibration*, Vol. 489, 2020. https://doi.org/10.1016/j.jsv.2020.115676.